# Spatial Control of Photoemitted Electron Beams using a Micro-Lens-Array Transverse-Shaping Technique

A. Halavanau[1,2], G. Qiang[3,4], G. Ha[5], E. Wisniewski[3], P. Piot[1,2], J. G. Power[3], W. Gai[3],
[1] Department of Physics and Northern Illinois Center for Accelerator & Detector Development, Northern Illinois University, DeKalb, IL 60115, USA
[2] Fermi National Accelerator Laboratory, Batavia, IL 60510, USA
[3] Argonne Wakefield Accelerator, Argonne National Laboratory, Lemont, IL, 60439, USA
[4] Accelerator laboratory, Department of Engineering Physics, Tsinghua University, Beijing, China
[5] POSTECH, Pohang, Kyoungbuk, 37673, Korea

(Dated: March 12, 2022)

A common issue encountered in photoemission electron sources used in electron accelerators is the transverse inhomogeneity of the laser distribution resulting from the laser-amplification process and often use of frequency up conversion in nonlinear crystals. A inhomogeneous laser distribution on the photocathode produces charged beams with lower beam quality. In this paper, we explore the possible use of microlens arrays (fly-eye light condensers) to dramatically improve the transverse uniformity of the drive laser pulse on UV photocathodes. We also demonstrate the use of such microlens arrays to generate transversely-modulated electron beams and present a possible application to diagnose the properties of a magnetized beam.

PACS numbers: 29.27.-a, 41.75.Fr, 41.85.-p, 42.15.Dp, 42.15.Eq, 42.30.Lr, 42.60.Jf

## I. INTRODUCTION

Photoemission electron sources are widespread and serve as backbones if an increasing number of applications including, e.g., high-energy particle accelerators, accelerator-based light sources, or ultra-fast electron diffraction setups. For a given photoemission electron - source design, the electron-beam properties, and notably its brightness, are ultimately limited by the emission process and especially the initial conditions set by the laser pulse impinging the photocathode. A challenge common to most applications is the ability to produce an electron beam with uniform transverse density. Non uniformities in the transverse electron-beam density can lead to transverse emittance dilution or intricate correlations. Producing and transporting a laser pulse while preserving a homogeneous transverse density is challenging and has been an active area of work [1]. For instance, the ultraviolet (UV) laser pulses typically employed for photoemission from metallic or semiconductor cathodes requires the use of nonlinear conversion process to form the UV pulse from an amplified infrared (IR) pulse. This frequency up-conversion mechanism often introduces transverse inhomogeneities owing to the nonlinearity of the conversion process.

In this paper, we investigate an alternative simple technique capable of controlling the transverse shape of a UV laser pulse. The technique employs microlens arrays (MLAs) to directly homogenize the UV laser pulse. MLAs are commonly employed as optical homogenizers for various applications [2–4]. In addition to its homogenizing capability, we also demonstrate that the MLA-based technique can also produced a periodic transverse pattern that can form a two-dimensional array of transversely-segmented beams. Such type of beams could find application in beam-based diagnostics of accelerator, single-shot quantum-efficiency map measurement, and coherent light sources in the THz regime or at shorter wavelength [5, 6].

In this paper, after briefly summarizing the principles of the MLA setup, we demonstrate its possible use to homogenize the ultraviolet (UV) laser spot of the photocathode drive laser. We especially establish the usefulness of MLAs to control the electron beam distribution in a series of experiments carried out at the Argonne Wakefield Accelerator (AWA) facility [7].

## II. OPTICAL PERFORMANCES OF THE MLA

Qualitatively, the principle of the MLA lies in redistributing the incoming light intensity across the light beam spot. Typically, MLAs are arranged in pairs. After passing through the MLA assembly, the light rays are collected by a "Fourier" lens which focuses parallel rays from different light beamlets to a single point at the image plane. Under proper conditions (distance to the Fourier lens and its focal length), the process leads to transverse homogenizing of the beam; see Fig. 1. Therefore the MLA homogenization scheme is rather simple and appealing in the context of photocathode drive lasers.

Alternatively, imaging the object plane of the single microlenses in the MLA with a "Fourier" lens produces a set of optical beamlets arranged as arrays (with a pattern mimicking the microlens spatial distributions).

### A. ABCD formalism

We first analyze the typical MLA setup diagrammed in Fig. 1 to derive a few salient features relevant to homogenization using the ABCD formalism [2]. We consider an initial ray to be characterized by the vector $(x_0, x_0')$, where $x_0$ and $x_0' \equiv \frac{dx_0}{dz}$ are respectively the initial ray position and divergence (here, $z$ represents the path-length along the optical transport). As a simple example, we consider a rectangular array of microlens in the $(x, y)$ plane with an equal pitch in both transverse directions. Using the ABCD formalism, and considering that the ray is within the aperture $\rho$ of the lens with center located at $(x = mp, y = np)$, we can describe the MLA with the linear transformation

$$\begin{pmatrix} x_1 - mp \\ x_1' \end{pmatrix} = \begin{pmatrix} 1 & 0 \\ -1/f_2 & 1 \end{pmatrix} \begin{pmatrix} 1 & s \\ 0 & 1 \end{pmatrix} \times \times \begin{pmatrix} 1 & 0 \\ -1/f_1 & 1 \end{pmatrix} \begin{pmatrix} x_0 - mp \\ x_0' \end{pmatrix}, \quad (1)$$

where $(x_1, x_1')$ is the ray vector after two MLA plates, $s$ is the spacing between two plates, $p$ is the array pitch, $f_1$ and $f_2$ are the focal lengths of the first and second microlens respectively. It should be pointed out that the ray initial and final coordinate satisfy $\sqrt{(x_0 - mp)^2 + (y_0 - np)^2} \leq \rho$ where $n$ and $m$ are integers that specify the position of each micro-lens in term of the pitch. Then, the output ray from the MLA setup can be further propagated up to the homogenization plane as

$$\begin{pmatrix} x_h \\ x_h' \end{pmatrix} = \begin{pmatrix} 1 & L \\ 0 & 1 \end{pmatrix} \begin{pmatrix} 1 & 0 \\ -1/F & 1 \end{pmatrix} \begin{pmatrix} 1 & d \\ 0 & 1 \end{pmatrix} \begin{pmatrix} x_1 \\ x_1' \end{pmatrix}, \quad (2)$$

where $(x_h, x_h')$ is the ray vector at the homogenization plane, $d$ the distance between the Fourier lens and the MLA, $F$ the focal length of the Fourier lens and $L$ is the distance to the homogenization plane.

From the formalism above one can deduce a few useful expressions. First, we consider the case when the two MLAs are identical ($f_1 = f_2 = f$) and located in the object plane of the Fourier lens ($L = F$). We further assume that there is no cross-talk between the microlens and their transformation only affects rays within a finite aperture smaller than the array pitch $\sqrt{(x_0 - mp)^2 + (y_0 - np)^2} \leq p/2$. Under these assumptions, we find the diameter of the image at the homogenization plane to be

$$D_h \approx \frac{Fp}{f^2}(2f - s) \quad (3)$$

in the limit of small ray divergence (as indicated by the independence of the equation on $d$). For practical purposes, we also calculate the diameter of the beam at the Fourier lens plane to be

$$A_F \approx \frac{dp}{f^2}(2f - s). \quad (4)$$

The latter equation is useful to estimate the required aperture.

In practice, the assumption $L = F$ might be challenging to satisfy. In such cases, the following expression is useful to find the beam size at a given location $L$ with respect to "Fourier" lens:

$$D(L) \approx \frac{pL}{f^2}(2f - s) + \frac{dp(2f - s)}{f^2}\frac{F - L}{F}. \quad (5)$$

If $L \approx F$ the resulting image remains homogenized due to the finite size of the Airy disk. Moving away from the focal plane increases the density modulations and eventually yield an array of beamlets.

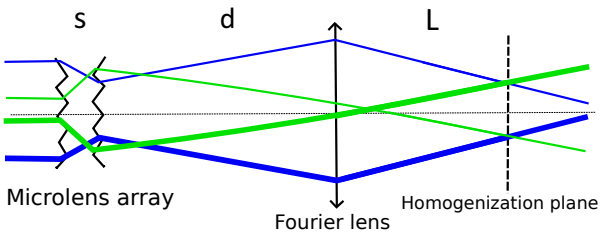


FIG. 1. Schematics of the microlens array configuration. Initial intensity fluctuations in the beam (thin/thick ray) becomes evenly distributed at the homogenization plane.

### B. Optical transport design

Photoinjector setups often incorporate relatively long (multi-meter scales) optical transport lines. The optical lines include transport from the laser room to the photoinjector enclosure (generally performed in the air or in moderate vacuum pipe) and the injection in the ultra-high-vacuum accelerator beamline up to the photocathode. Consequently, it is necessary to devise an optical transport line capable of imaging the homogenized laser profile on the photocathode surface. A commonly-used imaging setup, known as $4f$-imaging, is challenging to implement in the present case as it would require some of the lenses to be located in the vacuum chamber, as the "imaging" plane has to be much farther downstream than the "object" plane upstream.

However, imaging can be achieved in numerous ways while accommodating the various constraints related to MLAs (limited apertures, available focal lengths, etc...). To construct the appropriate optical line we impose the vector of a ray in the homogenization plane $(x_h, x_h')$ to be transported to a downstream imaging plane $(x_I, x_I')$ via

$$\begin{pmatrix} x_I \\ x_I' \end{pmatrix} = \mathbf{M} \begin{pmatrix} x_h \\ x_h' \end{pmatrix}, \quad \text{with} \quad \mathbf{M} = \begin{pmatrix} \mathcal{M} & 0 \\ 0 & 1/\mathcal{M} \end{pmatrix},$$

where the magnification $\mathcal{M}$ is set to 1 for one-to-one imaging. The latter linear system yields four equations;

an additional constraint comes from the total length of the imaging transport. Therefore, the problem has 5 unknowns in total with some flexibility within available lenses. Hence, it is possible to construct four-lens solution with distances between lenses as free parameters to make the corresponding system of linear equations well-defined.

The simulation of such a four-lens system was accomplished with a simple ray-tracing program where an initial set of optical ray were distributed according to a two-dimensional Gaussian distribution in the $(x, x')$ optical trace space. The optical layout of the laser transport downstream of the MLA is depicted in Fig. 2(a): it includes four cylindrical-symmetric lenses, an optical window that allows for the laser beam to be injected in an ultra-high-vacuum area and an in-vacuum metallic mirror that direct the laser beam on the cathode surface. The resulting evolution of the beam size along the transport downstream of the MLA and up to the photocathode is display in Fig. 2(a,b) for the two RF-gun configurations available at the AWA facility. For both setups, the large beam size produced at the location of the last optical lens demands a large-aperture lens. The beam size downstream of it gradually decreases until it reaches its target transverse size on the photocathode surface (8 mm rms). The in-vacuum mirror located close to the last optical transport lens can be another limiting aperture of the optical system and generally results in beam losses. For the two cases reported in Fig. 2 (a) and (b) the MLA-to-cathode transmission due to the finite geometric aperture, window transmission coefficient, losses in the lenses and mirrors was computed to be 57% and 43%.

The designs presented in the Fig. 2 were also simulated with the SYNCHROTRON RADIATION WORKSHOP (SRW software [8] which is based on Fourier optics and readily include a wave-propagation treatment of the laser transport; see Fig. 2 (c) inset. It confirmed that diffraction effects in the setup are negligible compared to transmission losses in the optical system. In the future, the established numerical model of the MLA will be used for customizing the micro-lens profiles, arrangement, and pitch. It should be noted that linearized ABCD approach is sufficient to set up MLA system and full wave propagation simulations may be omitted in the beginning.

Finally, transverse instabilities coming from shot-to-shot jitter in the transverse distribution displayed in Fig. 3 (left), would result in charge fluctuations if the laser beam is collimated by an iris upstream of the MLA. To improve the stability of the laser intensity we introduced a two-lens beam reducer in front of the MLA.

### C. Optical measurements

To evaluate the performance of the proposed scheme, we use two MLA's on the photocathode drive laser of the AWA [7]. The input UV ($\lambda = 248$ nm) laser pulse is obtained from frequency tripling of an amplified IR pulse originating from a Titanium-Sapphire (Ti:Sp) laser system. Downstream of the frequency tripler the UV pulse is further amplified in a two-pass excimer amplifier before transport to the accelerator vault. The setup shown in Fig. 1 was followed by the optical transport line shown in Fig. 2. A calibrated UV-sensitive screen with associated CCD camera mounted downstream of the setup directly provided a measurement of the achieved transverse distribution.

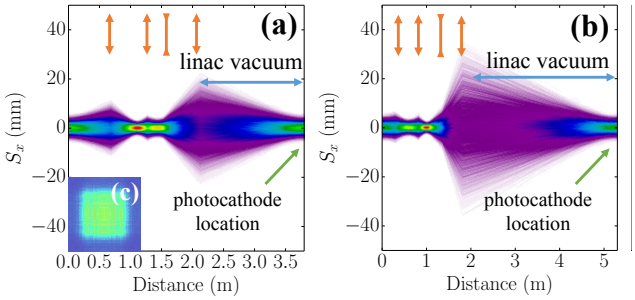


FIG. 2. False color ray-tracing distribution of a four-lens optical line capable of imaging the homogenized beam on the photocathode surface. The configuration in (a) and (b) correspond respectively to the AWA witness-beam and drive-beam electron-source setups. The lenses type and locations are shown as red arrows. The inset (c) gives the intensity distribution simulated using the ectorial-diffraction program SRW for a $5 \times 5$ rectangular MLA.

To gain confidence in the performances of the MLA setup, we first investigated the impact of a non perfectly collimated incoming laser beam. As it can be inferred from Fig. 1, the homogenization can still be achieved even if the incoming beam has a small divergence. There is a critical value of beam divergence $\tan\theta = p/2f$ that causes destructive interference after the MLA and results in light loss [9].

The beam size provided by Eq. 3 was used in the optical relay setup and Eq. 4 justified the aperture value of the "Fourier" lens. Overall, we have observed a good agreement with Eq. 3 and Eq. 4. The calculated laser beam size was within the aperture of all optical elements and latter was confirmed experimentally.

Note, that the Fourier lens in the experimental setup should be placed at the distance $D > F$ from the array, where $F$ is the focal length of the Fourier lens.

The setup was also employed to demonstrate the homogenization process and quantify its performances. The nominal UV laser pulse was used as a starting condition; see Fig.3(a). The inhomogeneity of the transverse distribution can be quantified using the spatial Fourier transform [10]. Correspondingly, we consider the digitized image $I(x, y)$ associated to the transverse laser distribution and compute its two-dimensional (2D) Fourier transform $\tilde{I}(k_x, k_y)$ using the fast-Fourier-tranform (FFT) al-

gorithm available in the PYTHON's NUMPY toolbox [11]. Here $k_x, k_y > 0$ are the spatial wavenumbers respectively associated to the horizontal and vertical direction. In order to simplify the comparison we further introduce the one-dimensional Fourier transform $\tilde{I}_x(k_x) = \int_0^{+\infty} \tilde{I}(k_x, k_y) dk_y$ along the horizontal axis [a similar definition hold for the vertical axis $\tilde{I}_y(k_y)$]. Figures 3 (d) and (g) respectively correspond to the 2D Fourier transform and the projection along the horizontal wavenumber $k_x$ axis associated to the laser distribution displayed in Fig. 3 (a). It displays typical microstructures observed in previous runs at AWA, and the corresponding spectrum displays some small modulations at low frequencies with most of the spectral content below $k_i < 5$ mm$^{-1}$. It should be noted that the excessive beam distortion observed in Fig. 3(a) is the result of beam filamentation as the high-energy UV pulse propagates in the 20-m open-air optical transport system from the laser room to the accelerator vault.

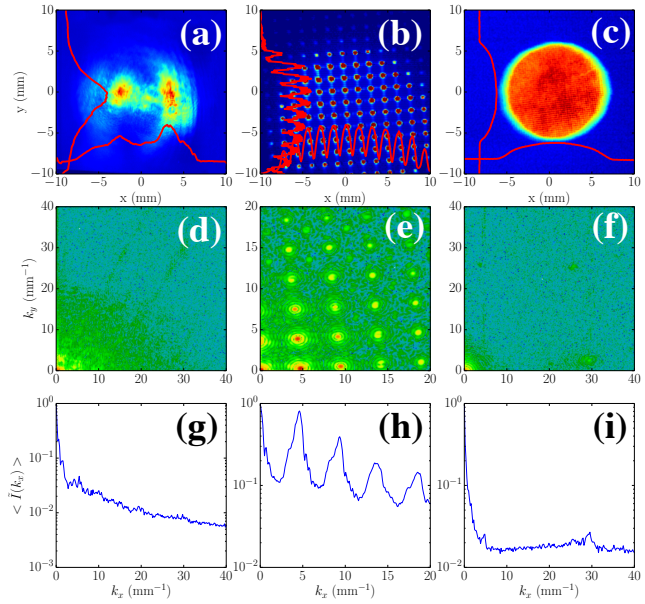


FIG. 3. Measured UV laser without MLA (left column) and with MLA setup to produce beamlets (middle column) or as a homogenizer (right column). The upper, middle and lower rows respectively correspond to the laser transverse density distribution, its 2D FFT, and the projected spectrum along the horizontal frequency $k_x$.

When the MLA setup is configured to homogenize the beam [see Fig. 3(c)], the Fourier transform indicates that the although the low frequency modulations seen in the original beam are suppressed, high-frequency modulations are present for $k_x > 12$ mm$^{-1}$. These modulations have a bunching factor on the order of $10^{-2}$ and correspond to very small modulation wavelength (<0.5 mm) barely observable on the distribution; see Fig. 4.

Additionally, the MLA can be arranged to form a

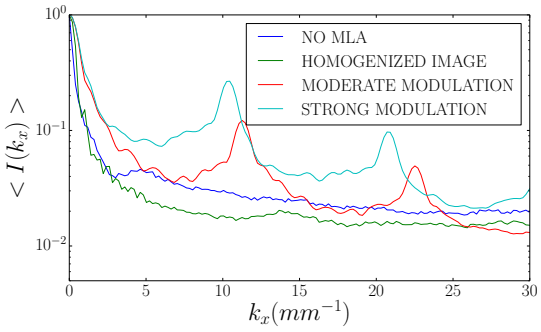


FIG. 4. FFT spectrum along the horizontal axis $\tilde{I}(k_x)$ for the different positions of the "Fourier" lens. The blue trace corresponds to no MLA case. The green, red, and turquoise traces respectively correspond to the "Fourier" lens located at 250, 275 and 325 mm from the MLA array.

transversely-modulated laser distribution, the spectrum indicates a bunching factor at frequencies larger than the characteristic frequency associated to the total beam size; see Fig. 3(b,e,h). We should point out that the non cylindrical-symmetric (square shaped) pattern transferred to the electron beam is eventually rotated due to the Larmor precession in the solenoidal lenses commonly surrounding RF guns. It is therefore important to mount the MLA assembling on a rotatable optical stage for remote control of the final pattern angle. Such an approach would decouple the downstream focusing (when solenoid are employed) and ensure the final distribution does not have significant coupling between the two transverse degrees of freedom. Additionally, the fine control over the rotation of the final distribution could be used to select rotation angles with higher-order bunching to reach higher modulation frequencies, e.g., before injecting the beam in a transverse-to-longitudinal phase space exchanger to map the modulation into the temporal domain.

Figure 4 compares the projected horizontal Fourier spectra for four cases of MLA configurations. Each spectrum is obtained by averaging five measurement taken after $f = 250$ mm Fourier lens at 250 mm, 275 mm and 325 mm to study the off-focal modulation and pattern formation. The latter Figure confirms that in homogenization regime MLA setup significantly improves the image spectrum by suppressing the original low-frequency modulations in the beam.

Finally, we quantify the laser power loss in the devised setup. The MLA plates employed in our series of experiment do not have any UV anti-reflection (AR) coating, hence the power loss was $\sim 5\%$ per surface totaling $\sim 20\%$ for the two MLAs. Additionally, the AR-coated UV lenses introduce a power loss of $\sim 2\%$ per lens. In our optical setup the laser energy was measured to be $4.2 \pm 0.1$ and $2.5 \pm 0.1$ mJ respectively upstream and downstream of the MLA setup including the Fourier and four trans-

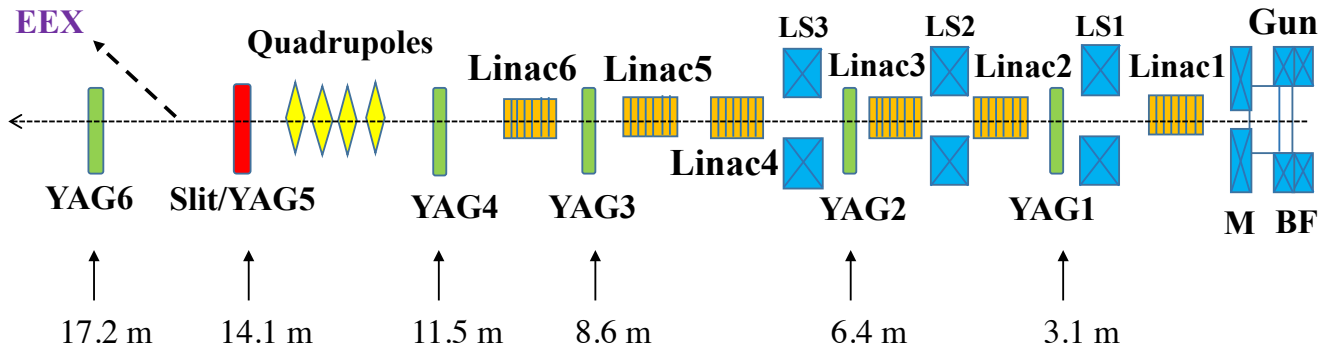


FIG. 5. Overview of the AWA-DB beamline only showing elements relevant to the performed experiment. Bucking-focusing (BF) and matching (M) solenoids were adjusted to image the beam on YAG screens. Linac solenoids (LS) and quadrupoles were turned off during the experiment. The positions of the YAG viewers are denoted in meters. The energy gain of one accelerating cavity (linac) is 10 MeV. EEX label marks the separate double-dogleg beamline for emittance exchange experiments

port lenses. Such a measurement indicates an energy transmission of $\sim 60\%$ which could most likely be further improved in an optimized setup. However given the UV laser energy available during our proof-of-principle experiment and the real-estate constraints we did not carry out such an optimization.

## III. APPLICATION OF THE MLA AS A LASER HOMOGENIZER

The first set of experiments consisted in demonstrating the simple homogenization technique to improve the emittance of an accelerator. The experiment was performed in the AWA "drive-beam" accelerator (AWA-DB) diagrammed in Fig. 5. In brief, the transversely manipulated UV laser pulse impinges a high-quantum efficiency Cesium Telluride ($Cs_2Te$) cathode located in an L-band (1.3-GHz) RF gun to produce 7 MeV electron bunch. The electron bunches are then further accelerated in an L-band normal conducting cavities up to 75 MeV. For a detailed description of the facility, the reader is referred to Ref. [7]. The RF gun is surrounded by three solenoidal lenses referred to as bucking, focusing and main solenoids. The bucking and focusing solenoid have opposite polarity and are ganged to ensure the axial magnetic field on the photocathode vanishes. Several YAG:Ce scintillating screen (YAG in Fig. 5) are available to measure the beam transverse density along the accelerator beamline.

### A. Beam dynamics simulations

We carried out several simulations using the beam-dynamics program General Particle Tracker (GPT) [12] to explore the impact of the MLA-homogenized beam on the resulting emittance. Transverse inhomogeneities on the laser distribution at the photocathode surface are mirrored on the photoemitted electron bunch distribution. These imperfection results in asymmetric space-charge forces and eventually yield phase-space dilution that ultimately degrade the beam emittances [13]. Therefore the homogenized laser beam is expected to improve the beam transverse emittance.

The initial macroparticle distribution was produced using a Monte-Carlo generator using the measured transverse distribution of the laser similarly to Ref. [14]. The temporal laser distribution is taken to be Gaussian with RMS duration $\sigma_t = 2.5$ ps, consistent with streak camera measurements. The momentum of the macroparticle assumes an excess kinetic energy of 0.5 eV as typically considered for $Cs_2Te$ cathodes [15]. We considered the nominal and homogenized laser distribution respectively shown in Fig. 3(a) and (c). To ensure a fair comparison, the total charge for both cases of distributions was set to 1 nC. Likewise, the RMS transverse sizes of the distribution was fixed to $\sigma_c = 8$ mm along both the horizontal and vertical directions. The simulations demonstrate that the beam transverse emittances are reduced by a factor $\sim 2$ for the case of the homogenized laser distribution; see simulated row in Table I and Fig. 6.

### B. Transverse emittance measurements

The experimental verification of the benefits of homogenizing the laser distribution was accomplished using the measured distribution of Fig. 3(a) and (c). For the homogenized distribution displayed in Fig. 3(c), a circular iris was used to clip the laser distribution and ensure it had the same rms value as in Fig. 3(a) $\sigma_c = 8 \pm 0.2$ mm. The resulting electron beam was transported through the nominal AWA-DB beamline and accelerated to $p = 48 \pm 0.5$ MeV/c. The corresponding electron-beam transverse distributions measured at YAG5 are compared in Fig. 7(a,b). The distribution originating from the initial (inhomogenized) does not present any distortion except

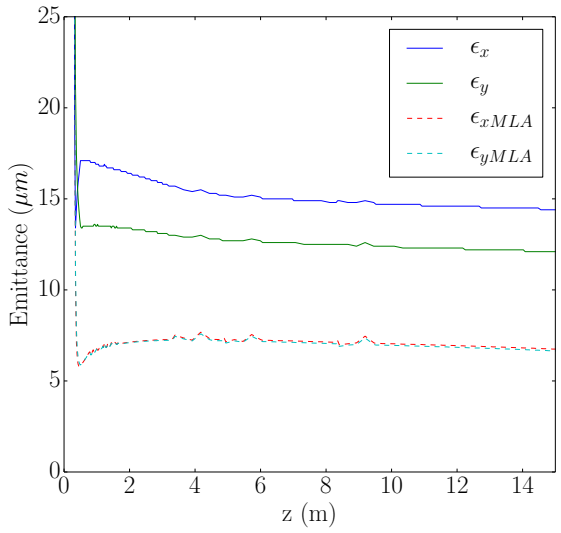


FIG. 6. Evolution of the transverse normalized emittances along the AWA-DB beamline simulated with GPT for a 1-nC bunch. The simulations were performed using as initial condition both the measured nominal (solid trace) and homogenized (MLA, dashed traces) laser distributions. The ordinate $z$ is the distance from the photocathode surface along the beamline.

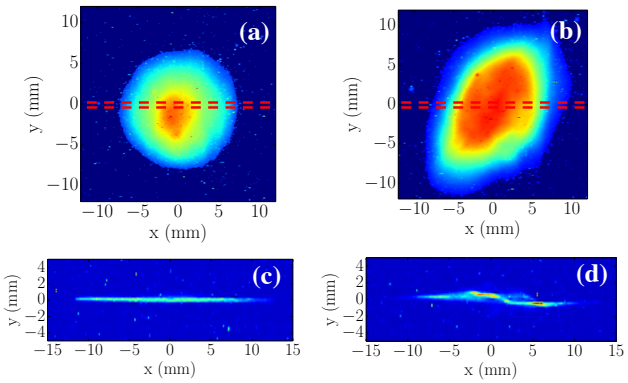


FIG. 7. Beam transverse distribution at YAG5 (a,b) and associated distribution of the beamlet transmitted through a horizontal slit located at YAG5 location and measured at YAG6 (c,d). The set of images (a,b) [resp. (c,d)] corresponds to the case when the MLA was inserted [resp. retracted] from the laser-beam path. The horizontal dash line in (a,b) represent the aperture of the slit.

for beam asymmetric and having some $x-y$ coupling. In contrast, the homogenized distribution is cylindrically symmetric and does not show any coupling. To further quantify the improvement we measured the beam vertical emittance using the slit technique. A 100-$\mu$m wide horizontal slit was inserted at YAG5 and the transmitted beamlet was observed 3.1 m downstream at YAG6 thereby providing the beam divergence $\sigma'_y$. Such a measurement together with the vertical beam-size measurement at YAG5 $\sigma_y$ provide an estimate of the normalized vertical emittance via $\varepsilon_y = \beta\gamma\sigma_y\sigma'_y$, where $\beta \approx 1$ and $\gamma = 93.9$. It should be stressed that the reported emittance is the core emittance and does not fully characterize the beam transverse phase space. Nevertheless this quantity provides a figure of merit to investigate the impact of the MLA on the beam quantity. The resulting beamlet distributions at YAG5/6 are shown in Fig. 7(b,d) and the measured divergence and resulting emittance compared in Tab. I.

| parameter | experimental conditions | | units |
|---|---|---|---|
| | No MLA | MLA | |
| Simulation with GPT | | | |
| momentum $\langle p \rangle$ | 48 | 48 | MeV/c |
| $\sigma_x$ | 3.6 | 3.8 | mm |
| $\sigma_y$ | 4.4 | 3.9 | mm |
| $\sigma'_x$ | 4.6 | 1.7 | $\times 10^{-2}$ mrd |
| $\sigma'_y$ | 3.1 | 1.5 | $\times 10^{-2}$ mrd |
| $\varepsilon_x$ | 15.6 | 6.1 | $\mu$m |
| $\varepsilon_y$ | 12.8 | 5.5 | $\mu$m |
| Measurement | | | |
| momentum $\langle p \rangle$ | 48 $\pm$ 0.5 | 48 $\pm$ 0.5 | MeV/c |
| $\sigma_x$ | 4.4 $\pm$ 0.2 | 4.0 $\pm$ 0.2 | mm |
| $\sigma_y$ | 5.2 $\pm$ 0.2 | 3.7 $\pm$ 0.2 | mm |
| $\sigma'_y$ | 4.2 $\pm$ 1.3 | 3.3 $\pm$ 1.0 | $\times 10^{-2}$ mrd |
| $\varepsilon_y$ | 20.5 $\pm$ 7.4 | 11.6 $\pm$ 4.3 | $\mu$m |

TABLE I. Comparison between measured and simulated beam parameters at YAG5 for $Q = 1\pm0.1$ nC. The experimental setup only allowed for the vertical normalized emittance to be measured. The parameters are all given as RMS quantities and corresponds to the distributions shown in Fig. 7.

The resulting emittances are comparable with the value simulated with GPT (Fig. 6) and indicate a factor $\sim 2$ improvement for when the homogenized laser beam is employed. The relatively large error bars in Tab. I are due to hardware uncertainty (mostly the slit width). It should be noted that the errors between the two measurements are correlated, i.e. the uncertainty leds to the upper (resp. lower) value for simultaneously the "MLA" and "No MLA" measurements, thereby giving confidence, despite the large error bar on the emittance, that the emittance reduces when the MLA is used to homogenize the laser beam. It should finally be pointed out that the reported emittance were produced with a nominal setup of the AWA-DB beamline, i.e. no emittance-minimization technique was attempted prior to the measurements.

## IV. PRODUCTION AND TRANSPORT OF MULTI-BEAM ARRAYS

The application of the MLA setup investigated below is the formation of transversely-segmented beams – i.e. consisting of an array of beamlets. Such a distribution

could have a variety of applications such as described in Refs. [16, 17]. Alternatively, the formed array could produce a transversely modulated beam that could be injected in a transverse-to-longitudinal phase-space exchanger to yield a temporally-modulated beam [18, 19]. The latter opportunity motivated the present work to demonstrate the generation and preservation of an array of beamlets up to the entrance of a transverse-to-longitudinal phase-space exchanger installed in the AWA-DB [20] and recently employed for temporal shaping [21]. Additionally, the multi-beam may serve as a beam-based diagnostic tool, e.g., to investigate nonlinearities of the externally-applied electromagnetic field or measure transfer matrices of beamline elements. In this section, we explore whether the beam transverse electron-beam modulation originating from the laser is preserved during the photoemission processes and low-energy acceleration in the RF gun.

### A. Beam dynamics simulations

Using the particle tracking codes GPT and IMPACT-T [22] we performed simulation of the AWA-DB RF-gun beam dynamics. The preservation of the modulation is affected by space-charge forces which play a dominant role in the beam dynamics in the vicinity of the cathode and in the RF gun. Given the multi-scale nature of our problem, the space-charge forces are computed with a Barnes-Hut (BH) algorithm [23] available in GPT. Similar algorithm was successfully tested in recent studies [24, 25].

The measured transversely-modulated laser distribution at the photocathode location [similar to Fig. 3(b)] was used to generate the input macroparticle distribution for our numerical simulations. An initial intent was to probe whether the modulation could possibly be amplified via collective effects (e.g. implying transverse space charge modulations that will eventually convert into energy modulations) or if they are simply smeared out via thermal-emittance effect as the beam is photo-emitted. The beamlet pattern was also used to ensure the GPT model could reproduce our experimental observation at low energy (RF-gun only). We compare the simulated and measured transverse patterns for different matching-solenoid current settings in Fig. 8. The beam data and numerical simulations were recorded downstream of the gun using YAG1 at a beam energy of $7 \pm 0.5$ MeV and bunch charge was set to 150 pC. The observed pattern rotation indicates that the Larmor angle which depends on the beam energy and applied magnetic field agrees qualitatively with the simulation; see Fig. 8. The observed discrepancy is caused by the uncertainties on the RF-gun field RF uncertainties in the RF-gun.

### B. Multi-beam formation downstream

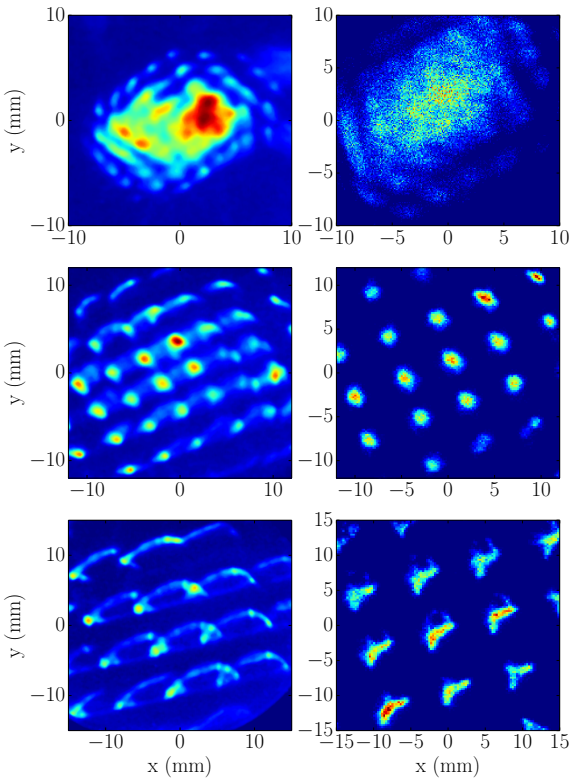


FIG. 8. Measured (left) and simulated (right) Q=100 pC electron-beam distribution at YAG1 when the UV laser pulse is modulated with the MLA array. The rows correspond to different matching-solenoid current settings of 215 A (upper row), 230 A (middle row) and 290 A (lower row).

### of the RF gun

A subsequent experiment investigated the formation of a beamlet array downstream of the RF gun at an energy of $7 \pm 0.5$ MeV for various operating points of the photoinjector. The incoming laser spot size on the MLA array was chosen to yield an $8 \times 8$ beamlet array. The photoemitted electron beam was observed on the YAG:Ce scintillating screen (YAG1 in Fig 5) located at $z = 3.1$ m from the photocathode surface. Figure 9 displays a sequence of beam distribution recorded at YAG1 for different settings of the focusing-bucking and matching solenoids. Note, that due to the surface space charge effects, the charge associated to each beamlet, and therefore the total maximum charge of the patterned beam, is limited. The total maximum charge of the patterned beam was measured to be approximately $\sim 15$ nC corresponding to an average charge of $\sim$ (15 nC)/$(8 \times 8) \simeq$ 200 pC per beamlet.

The resulting electron beamlet formations pictured on Fig. 9 were analyzed using the same Fourier analysis as

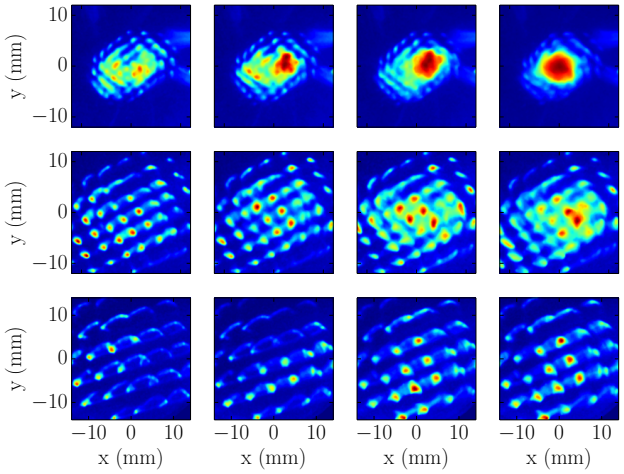


FIG. 9. False color measured 7 MeV electron beam patterns for various matching solenoid current setting and charge. From left to right: Q=60pC, 80pC, 100pC, 120pC. The images from top to bottom correspond to matching-solenoid currents of 215, 240, and 270 A.

the one used in Section II C for the UV-laser images. Figure 10 (a) summarizes the evolution of the transverse bunching factor at its lowest-frequency maximum versus total bunch charge for different matching solenoid settings. The average beamlet separation $d$ changes from 0.4 mm to 8 mm at YAG1 location with the matching solenoid current increased from 215 A to 270 A. Figure 10 (b) gives the evolution of the transverse bunching factor for the case of $d = 10 \pm 0.4$ mm. One can see the modulation is fully determined by solenoid imaging at charges of $Q < 180$ pC.

Finally, it should be noted, that the measurements were taken at YAG1 and do not provide information on possible modulation reappearance at a downstream position along the beamline: the betatron phase advance at a downstream observation point could be such that the modulation is washed out in the position space but prominent in the angular coordinate.

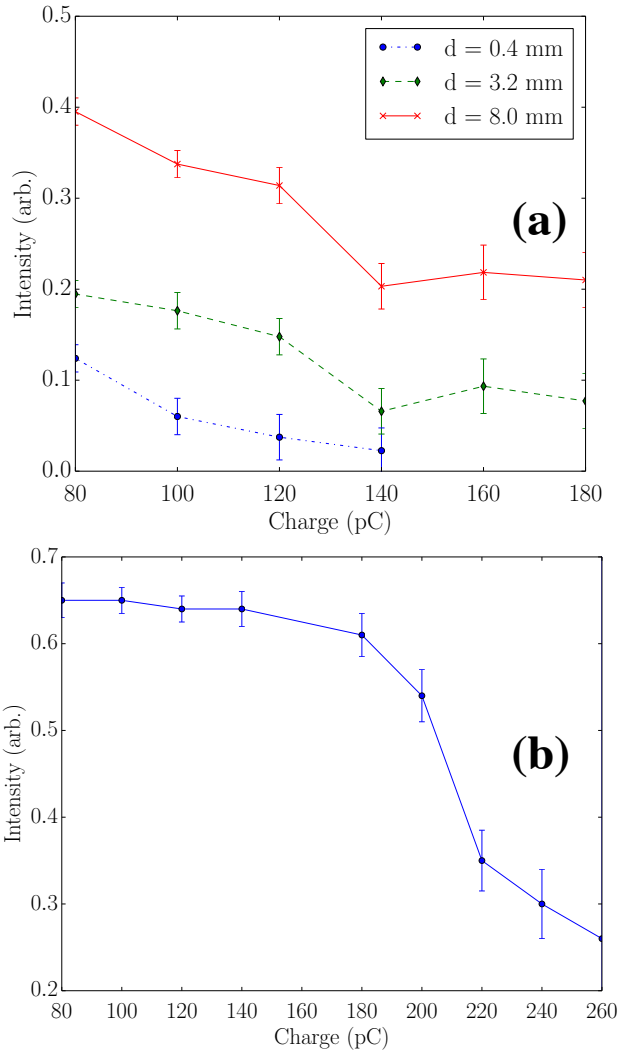


FIG. 10. Transverse bunching factor evaluated at its lowest-frequency maximum versus bunch charge for the three cases of solenoid settings displayed in Fig. 9 with corresponding beamlet spacing $d$ (a) and for the case of a solenoid field of 290 A with associated beamlet spacing of $d = 10$ mm (b).

### C. Multi-beam acceleration to 48 MeV

The modulation introduced on the cathode propagated and preserved through the beamline up to the transverse-to-longitudinal emittance-exchange (EEX) beamline entrance; see Fig. 11. There should be no strong focusing applied along the low-energy beamline as close encounter of the beamlets produces strong distortion as explored in Ref. [14]. Consequently, the low-energy beamline elements should be properly matched to allow the large waist. At medium energy, the transverse space-charge force is significantly decreased and therefore not expected to impact the multi-beam dynamics. In order to avoid a tight waist at low energy we used the linac solenoid LS1 (see Fig. 5) to image the beamlet pattern directly on the YAG5 screen located 14 m downstream of the photocathode surface and just prior to the EEX beamline. At this location, the beam energy is measured to be 48 MeV. Figure 11 shows the beam distribution at YAG5 for different bunch charge. The typical beamlets separation (center to center) is on the order of $\sim 3$ mm $\pm 0.3$ mm. Such a distribution could be further manipulated using a telescope composed of four quadrupole magnets to generate a train of short bunches along the temporal axis downstream of the EEX beamline [21]. Such bunch train could possibly support the generation of THz radiation using, e.g., coherent transition radiation, or the resonant excitation of wakefields in a wakefield structured such as

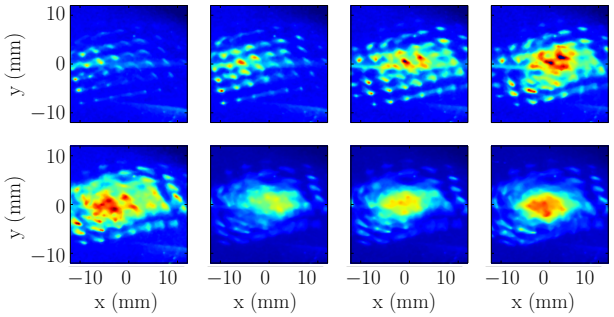


FIG. 11. False color measured 48 MeV electron beam patterns for various charges. From left to right and top to bottom: $Q = 60$, 100, 200, 300, 400, 500, 600, 700 pC with a matching-solenoid current of 240 A.

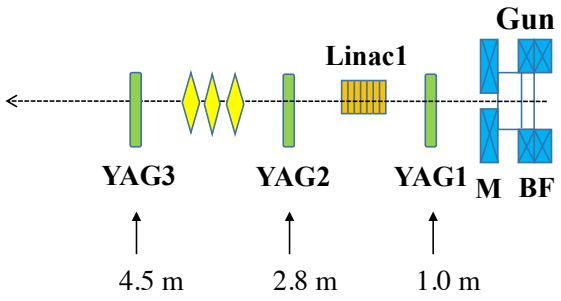


FIG. 12. Overview of the AWA-WB beamline. The bucking (B) and focusing (F) solenoidal lenses can be setup to produce CAM-dominated beams. The positions of the YAG viewers are denoted in meters.

a dielectric-lined waveguide [26]. As already noted, the coupling at YAG5 could be removed by mounting the MLA assembly on a rotatable mount. Likewise, the coupling could be taken advantage of to select an angle so that a smaller projected separation along the horizontal axis could be achieved. Such a configuration would provide a knob to continuously vary the beamlets separation (e.g. and THz-enhancement frequency) downstream of the EEX beamline.

## V. GENERATION OF MAGNETIZED MULTI-BEAMS

In this section, we describe a possible applications of the patterned electron beam form by the MLA setup as a beam-based diagnostic tool for inferring the residual axial magnetic field at the photocathode plate by measuring the value of canonical angular momentum (CAM).

As an example we consider the Argonne Wakefield Accelerator "witness-beam" (AWA-WB) beamline diagrammed in Fig. 12. In brief, AWA-WB accelerator incorporates an L-band $1 + \frac{1}{2}$ RF gun with a Mg photocathode on its back plate. The gun is surrounded by a bucking and focusing solenoids, nominally powered to yield a vanishing magnetic field $B_{0z}$ at the photocathode surface. The solenoids can be tuned and provide a non-vanishing axial magnetic field $B_{0z}$ at the cathode. Nominally, the bucking and focusing solenoids have the opposite polarity, however they can be operated with the same polarity and provide significant field ($B_{0z} \sim 0.1$ T) on the photocathode.

### A. Magnetized beams

According to Busch's theorem the total canonical angular momentum of an electron in an cylindrical-symmetric magnetic field is conserved and given by [27]

$$L = \gamma m r^2 \dot{\theta} + \frac{1}{2} e B_z(z) r^2 + \mathcal{O}(r^4), \tag{6}$$

where $(r, \theta, z)$ refers to the electron transverse position the cylindrical coordinate system. When a electron beam is born in presence of an axial magnetic field, it forms a "magnetized" beam state. Such beams have a variety of applications in electron cooling and can be further manipulated to form beams with asymmetric transverse emittances or "flat" beams [28].

The conservation of the CAM $L$ from Eq. 6 yields the mechanical angular momentum (MAM) of the beam in the magnetic-field-free zone to be

$$|\boldsymbol{L}| = \gamma m |\boldsymbol{r} \times \frac{d\boldsymbol{r}}{dt}| = \frac{1}{2} e B_{0z} r_0^2, \tag{7}$$

where $B_{0z}$ is the field at the cathode surface, $r_0$ and $r$ are respectively the electron radial coordinate on the photocathode surface and at a downstream magnetic-field-free location. The norm of $L \equiv |\boldsymbol{L}|$ can be computed as $L = |\boldsymbol{r} \times \boldsymbol{p}| = |x p_y - y p_x|$. Following Ref. [29], we characterize a CAM-dominated beam via its magnetization $\mathcal{L} \equiv \langle L \rangle / 2\gamma mc$ where $\langle L \rangle = e B_{0z} \sigma_0^2$ represents the statistical averaging of $L$ over the beam transverse distribution and $\sigma_0$ the RMS transverse radius of the electron beam on the photocathode surface.

### B. Method to measure $\mathcal{L}$

We now consider the multi-beam laser distribution discussed in Section IV impinging a photocathode immersed in an axial magnetic field. The resulting electron beam, composed of multiple beamlets, is born with a CAM and will therefore undergo a similarity transformation (in the presence of a axisymmetric external focusing) of the form

$$\begin{pmatrix} x \\ y \end{pmatrix} = [k + R(\theta)] \begin{pmatrix} x_c \\ y_c \end{pmatrix}, \tag{8}$$

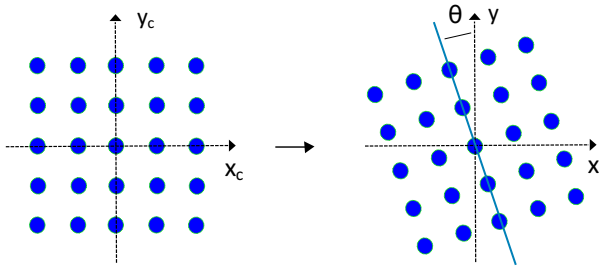


FIG. 13. Illustration of the similarity transformation between the initial beamlet pattern emitted from the phtocathode (left)as it propagates to a downstream location (right). This schematics assumes the transverse momentum is solely angular in an axisymmetric external-focusing lattice.

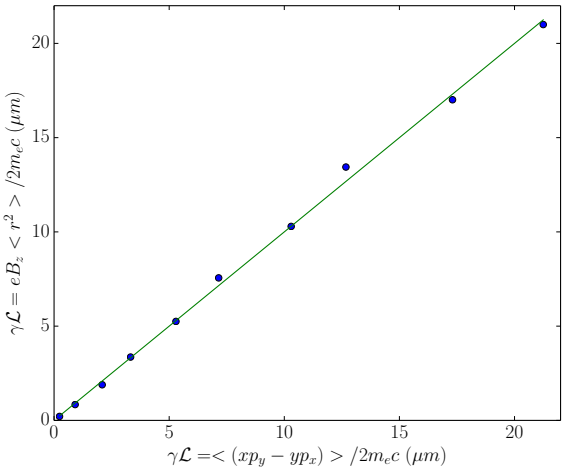


FIG. 14. Proof-of-principle via numerical simulations using IMPACT-T of the measurement method based on Eq. 9. The magnetization $\mathcal{L}$ is computed from the particle distribution (blue markers) and plotted against the magnetization inferred from the $B_{0z}$ on the cathode surface. The green solid line correspond to the diagonal line.

after exiting the magnetic-field region; see Fig. 13. In the previous equation the subscript $_c$ corresponds to the spatial coordinates on the cathode surface, $k$ is a scalar and $R(\theta)$ is the $2\times 2$ matrix associated to a rotation with angle $\theta$.

A measurement of the rotation angle and array size provides the value of mechanical angular momentum. [30] Such a measurement relies on the measurement of the pattern evolution between two axial locations. Considering two YAG:Ce screens separated by a drift space with length $D$, the mechanical angular momentum $L$ can then be deduced by computing the relative rotation of the beamlet pattern $\theta$ between the two locations as [31]

$$L = \frac{p_z}{D}\left[\left(\frac{n}{2}a_1\right)\right]^2 (M\sin\theta), \tag{9}$$

where $p_z$ is the axial momentum, $n$ is a number of beamlets, $a_1$ is the separation between beamlets at the first viewer, and $M = a_2/a_1$ is the magnification factor between second and first viewer. Relating it to Eq. 7 one can infer the value of the magnetic field on the cathode $B_{0z}$.

To validate the proposed method via numerical simulations we used IMPACT-T [22] and considered the AWA-WB beamline diagrammed in Fig. 12. Laser multi-beam array was converted into IMPACT-T particle distribution using the method described in Section III. It was then propagated through the beamline and saved at two locations of YAG screens (YAG2 and YAG3 in Fig. 12) and away from the waist. The centroids of each beamlet were found and the mechanical angular momentum is inferred from Eq. 9. We performed numerical simulations for different $B_{0z}$ field values and results are summarized in Fig. 14.

The latter Figure confirms that the CAM (as inferred from the value of $B_{0z}$) is fully transferred to the MAM. Some systematic discrepancies ($< 5\%$) are observed as $\mathcal{L}$ increases and most likely due to the contribution of nonlinear terms in multipole expansion of $B(z)$ not accounted for in Eq. 6 (which assumes a paraxial linear approximation). Likewise, space-charge effects might alter the results. Both limitations will be the object of further studies. Nevertheless, the simulations demonstrate that illuminated cathode with a patterned laser beam provides a simple method to measure the MAM. It should be noted, that the fundamental systematic error may also come from diagnostic cameras mutual misalignment. In a case of low $\mathcal{L}$, a longer distance between two screens has to be employed. Additionally, this technique provides an excellent determination of the magnetic axis and probes the laser spot alignment.

To extract the rotation angle and the beamlet separation, one can calculate beamlet positions using conventional 2D peak finding algorithm. However, this method becomes not very robust when the beamlet formation size at the location of the second screen is bigger than the screen size.

Another approach is to utilize projections $\langle\tilde{I}(k_x)\rangle$ and $\langle\tilde{I}(k_y)\rangle$ of the images in reciprocal Fourier space calculated via 2D fast Fourier transform (FFT). In this case, the tilt of the image will result in a difference between the locations of first harmonics; see Fig. 15. The tilt angle can be then computed as $\tan\theta = k_{x_1}/k_{y_1}$, where $k_{(x,y)_1}$ is the coordinate of the first-harmonic peak of the spatial bunching factor along the corresponding axis. Such an analysis assumes the beamlet-pattern periodicity along the two directions is identical (which is the case in our experiment). The full-width half-maximum (FWHM) sizes of the peaks in Fig. 15 are then accounted as errorbars of the measurement.

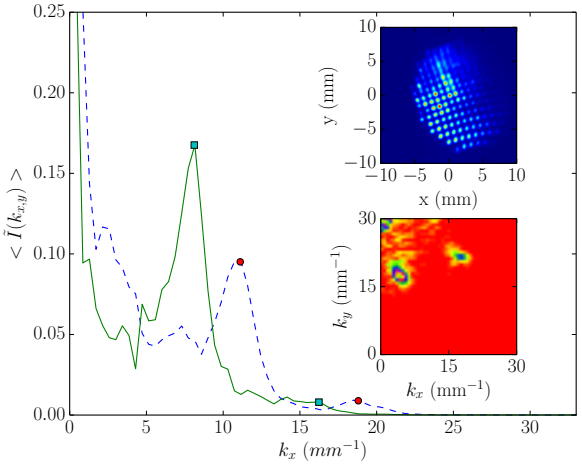


FIG. 15. Bunching factor as function of horizontal $k_x$ (solid trace) and vertical $k_y$ (dashed trace) spatial frequency. The ratio of the lowest-frequency peaks $k_{y1}/k_{x1}$ provides a measurement of the pattern rotation angle with respect to the horizontal axis. This data is extracted from the corresponding beam image (upper inset) and from projections of its 2D FFT image (lower inset).

### C. Electron beam experiment

Proof-of-principle electron beam experiment was performed at AWA-WBA beamline. A $12 \times 12$ laser beamlet pattern with rms duration of 6 ps was formed by using the technique from Section IV. The $\sim$ 5-MeV beam out of the RF gun was further accelerated using the L-band linac to $\sim$ 10 MeV; see Fig. 12. In the experiment, the total charge was 60 pC per bunch, resulting in $\sim$ 420 fC per beamlet.

The three solenoids depicted in Fig. 12 were controlled independently via unipolar power supplies. We started with the normal operational configuration where the bucking and focusing solenoids had opposite polarities which yields relatively low magnetization of the beam. The bucking solenoid current was slowly decreased to 0 A and the induced rotation of the beamlet formation was observed at YAG1 and YAG2 locations; see Fig. 16. Then the polarity of the bucking and focusing solenoids was flipped and the bucking solenoid current was ramped up to -500A. Total of 20 bucking solenoid current values were used to reach the maximum field at the cathode surface of $\simeq$ 1400 G.

The beamlet pattern at the two screens YAG1 and YAG2 makes a different rotation angle. The rotation of the pattern between the two screens $\theta$ increases with the magnetization, as it can be seen in Fig. 17. In the latter picture the data point were obtained from the 2D FFT technique detailed in the previous Section. From the inferred rotation angle $\theta$, the MAM was recovered via Eq. 9.

The retrieved value of the $B_{0z}$, the applied field on the cathode surface, computed using the data of Fig. 17 for different currents of the bucking solenoids are reported in Fig. 18. Specifically, the retrieved values are computed via $B_{z0} = \frac{2m_e c^2 L}{ec} r^2$ where $L$ is found from Eq. 9. These values are in very good agreement with sc impact-t simulations of the measurement which includes a model of the solenoids simulated with POISSON [32].

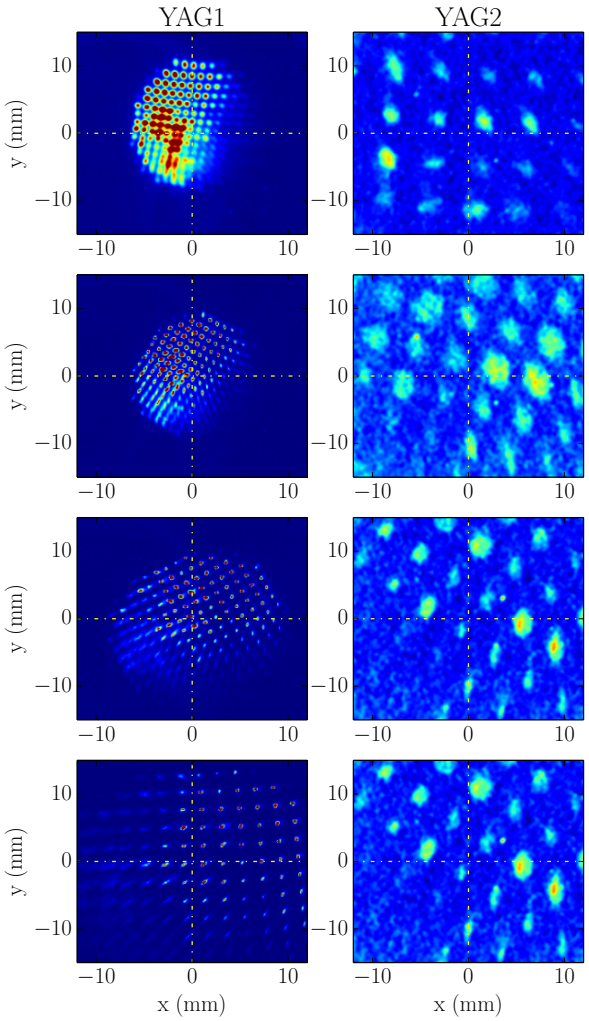


FIG. 16. Beamlet-pattern distribution on YAG1 (left column) and YAG2 (right column) for different settings of the magnetic field on the photocathode $B_{0z} = 0$, 200, 500, 1000 G (from top to bottom). The radial momentum (compared to the assumption made in the diagram of Fig. 13) yields to substantial magnification at YAG2 in addition to the rotation.

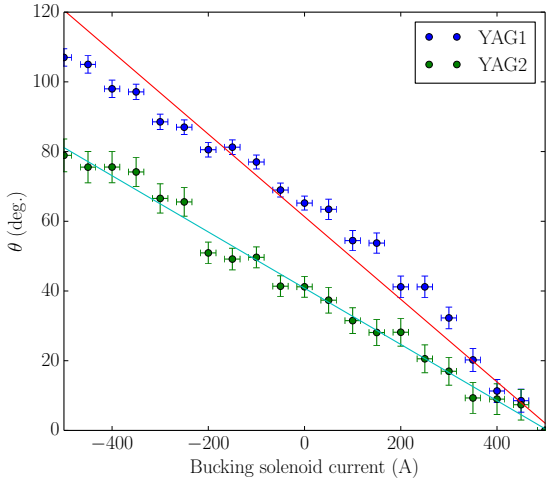


FIG. 17. Rotation angle of the beamlet pattern with respect to the vertical angle at screens YAG1 (left) and YAG2 (right) as function of the bucking-solenoid magnetic field. The lines correspond to a linear regression of the experimental data.

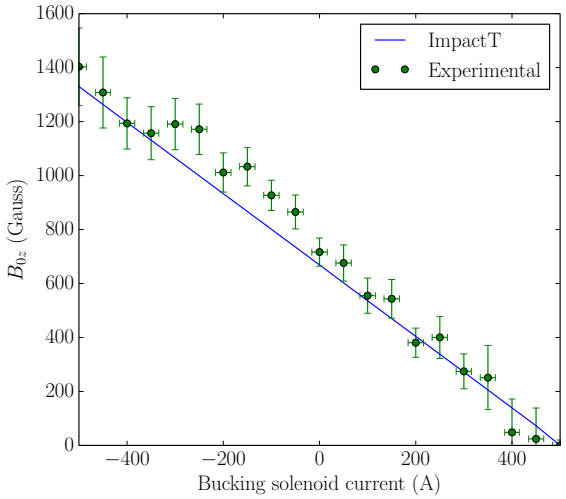


FIG. 18. Comparison between IMPACT-T simulations (solid blue line) and experimentally recovered values of $B_{0z}$ (symbols with error bars) from Fig. 16.

## VI. SUMMARY

We demonstrated the possible use of a microlens array to control the transverse distribution of a photocathode laser pulse and associated photoemitted electron bunches. We especially confirm that this simple and rather inexpensive setup could be used to homogenize the beam transverse distribution thereby improving the transverse emittance. Additionally, we investigated the generation of patterned electron beams consisting of multiple transversely-separated beamlets. The latter type of beam could be used for various application and could yield temporally-modulated electron beam when combined with a transverse-to-longitudinal emittance-exchange beamline but also serve as a beam-based diagnostics. We illustrated the application of the patterned beam to diagnose the magnetization of a magnetized beam (by using the beam evolution to infer the the axial magnetic applied at the photocathode surface). The application of patterned beams could be further extended to explore, e.g, nonlinearities in linear accelerators and characterize beamline element (transfer matrix measurement). Given its simplicity, low cost and versatility we expect the present work to motivate further applications to photoemission electron sources and laser-heater system.

## VII. ACKNOWLEDGEMENTS

This work was supported by the US Department of Energy under contract No. DE-SC0011831 with Northern Illinois University. The work by the AWA group is funded through the U.S. Department of Energy, Office of Science, under contract No. DE-AC02-06CH11357. The work of A.H. and partially P.P. is supported by the US Department of Energy under contract No. DE-AC02-07CH11359 with Fermi Research Alliance, LLC.

[1] S. Li, D.K. Bohler, W.J. Corbett, A.S. Fisher, S. Gilevich, Z. Huang, A. Li, D.F. Ratner, J. Robinson, F. Zhou, "LCLS Injector Laser Modulation to Improve FEL Operation Efficiency and Performance", Proceedings of the 2015 International Particle Accelerator Conference (IPAC15), JACoW, Richmond, Virginia, USA, paper TUPJE074 (2015).

[2] P. Schreiber, S. Kudaev, P. Dannberg, U. D. Zeitner, "Homogeneous led-illumination using microlens arrays", Proceedings of SPIE, **5942** (2005).

[3] F.M. Dickey and S.C. Holswade, *Laser Beam Shaping: Theory and Techniques*, Optical Science and Engineering, Taylor & Francis (2000).

[4] O. G. de Oliveira and D. W. de Lima Monteiro, "Optimization of the hartmann-shack microlens array", Optics and Lasers in Engineering, **49** (4), 521-525 (2011).

[5] Y. Shibata, T. Takahashi, T. Kanai, K. Ishi, M. Ikezawa, J. Ohkuma, S. Okuda, T. Okada, "Diagnostics of an electron beam of a linear accelerator using coherent transition radiation", Phys. Rev. E, **50**, 1479-1484 (1994).

[6] W. S. Graves, F. X. Kärtner, D. E. Moncton, and P. Piot, "Intense Superradiant X Rays from a Compact Source Using a Nanocathode Array and Emittance Exchange", Phys. Rev. Lett., **108**, 263904 (2012).

[7] J.G. Power, M.E. Conde, W. Gai, Z. Li, D. Mihalcea, "Upgrade of the Drive LINAC for the AWA Facility Dielectric Two-Beam Accelerator", Proceedings of the 2010 International Particle Accelerator Conference (IPAC10), JACoW, Kyoto, Japan, paper THPD016 (2010).

[8] O. Chubar, A. Fluerasu, L. Berman, K. Kaznatcheev, and L. Wiegart, "Wavefront propagation simulations for beamlines and experiments with SRW", J. Phys. Conf. Ser., **425**, 162001 (2013).

[9] SUSS MicroOptics techinfo sheet 10, "Beam homogenizing", (2008).

[10] We note another popular technique to quantify the quality of an optical beam relies on the decomposition into Zernike's polynomials. Our choice to use the two-dimensional Fourier transform was motivated by the need to use one figure of merit to quantify *both* the quality of the homogenized beam and to also parameterized the modulated beam.

[11] Python NUMPY library.

[12] S.B. van der Geer, *et al,* "3D space-charge model for GPT simulations of high brightness electron bunches", Institute of Physics Conference Series, **175**, 101 (2005).

[13] F. Zhou, I. Ben-Zvi, M. Babzien, X. Y. Chang, A. Doyuran, R. Malone, X. J. Wang, and V. Yakimenko, "Experimental characterization of emittance growth induced by the nonuniform transverse laser distribution in a photoinjector", Phys. Rev. ST Accel. Beams, **5**, 094203 (2002).

[14] M. Rihaoui, P. Piot, J. G. Power, Z. Yusof, and W. Gai. "Observation and simulation of space-charge effects in a radio-frequency photoinjector using a transverse multi-beamlet distribution", Phys. Rev. ST Accel. Beams, **12**, 124201 (2009).

[15] K. Flottmann "Note on the thermal emittance of electrons emitted by cesium telluride photocathodes", report DESY-TESLA-FEL-97-01, (1997).

[16] V. Marx, "Neurobiology: Brain mapping in high resolution", Nature, **503**, 147-152 (2013).

[17] Y. Yoshida H. Kashima K. Kan K. Norizawa A. Ogata S. Tagawa T. Kondoh, J. Yang. Spatial resolution and contrast of the intensity modulated electron beam by the photocathode rf gun for the radiation therapy. *Proceedings of EPAC08, Genoa, Italy*, page tupp121.

[18] P. Piot, Y.-E Sun, J. G. Power, and M. Rihaoui. "Generation of relativistic electron bunches with arbitrary current distribution via transverse-to-longitudinal phase space exchange", Phys. Rev. ST Accel. Beams, **14**, 022801 (2011).

[19] Y.-E Sun, P. Piot, A. Johnson, A. H. Lumpkin, T. J. Maxwell, J. Ruan, and R. Thurman-Keup, "Tunable subpicosecond electron-bunch-train generation using a transverse-to-longitudinal phase-space exchange technique", Phys. Rev. Lett., **105**, 234801 (2010).

[20] Y. E. Sun, J. G. Power, K. J. Kim, P. Piot, and M. M. Rihaoui, "Design study of a transverse-to-longitudinal emittance exchange proof-of-principle experiment", Proceedings of 2007 Particle Accelerator Conference (PAC07), JACoW, pages 3441-3443 (2007).

[21] G. Ha, M. H. Cho, W. Namkung, J. G. Power, D. S. Doran, E. E. Wisniewski, M. Conde, W. Gai, W. Liu, C. Whiteford, Q. Gao, K.-J. Kim, A. Zholents, Y.-E Sun, C. Jing, and P. Piot, "Precision control of the electron longitudinal bunch shape using an emittance-exchange beam line", Phys. Rev. Lett., **118**, 104801 (2017).

[22] J. Qiang, IMPACT-T reference manual. report LBNL-62326 (2007).

[23] J. Barnes and P. Hut, "A hierarchical O(N log N) force-calculation algorithm", Nature, **324**, 446-449 (1986).

[24] J.M. Maxson, I.V. Bazarov, W. Wan, H.A. Padmore, and C.E. Coleman-Smith, "Fundamental photoemission brightness limit from disorder induced heating", New Journal of Physics, **15** (10), 103024 (2013).

[25] A. Halavanau and P. Piot, "Simulation of a cascaded longitudinal space charge amplifier for coherent radiation generation", Nuclear Instruments and Methods in Physics Research Section A, **819**, 144-153 (2016).

[26] G. Qiang, C. Jing, S. Antipov, J. Shi, H. Chen, W Gai, J. Power, M. Conde, C. Whiteford, E. Wisniewski, W. Liu, D. Doran, "Transformer ratio enhancement experiment based on emittance exchanger in Argonne Wakefield Accelerator", Proceedings of the 2016 Northern American Particle Accelerator Conference (NAPAC16), JACoW, Chicago, IL, USA, paper THPOA08 (in press, 2016).

[27] M. Reiser. *Theory and design of charged particle beams*, Wiley, New York (1995).

[28] R. Brinkmann, Ya. Derbenev, and K. Flottmann. "A low emittance, flat-beam electron source for linear colliders", Phys. Rev. ST Accel. Beams, **4** ,053501 (2001).

[29] K. J. Kim. "Round-to-flat transformation of angular-momentum-dominated beams", Phys. Rev. ST Accel. Beams, **6**, 104002 (2003).

[30] A similar method was discussed in Ref. [31] for the case of slits located downstream of the electron source.

[31] Y. E Sun, P. Piot, K. J. Kim, N. Barov, S. Lidia, J. Santucci, R. Tikhoplav, and J. Wennerberg. "Generation of angular-momentum-dominated electron beams from a photoinjector", Phys. Rev. ST Accel. Beams, **7**, 123501 (2004).

[32] J. H. Billen and L. M. Young, in Proceedings of the 1993 Particle Accelerator Conference, Washington DC (IEEE, Piscataway, NJ, 1993), pp. 790-792